Contents lists available at ScienceDirect

Engineering Structures

journal homepage: www.elsevier.com/locate/engstruct

Behaviour of prestressed hollow core slabs strengthened with NSM CFRP strips around openings: A finite element investigation

Omar Elharouney *, Mahmoud Elkateb, Ayman Khalil

Structural Engineering Department, Ain Shams University, Cairo, Egypt

ARTICLE INFO

Keywords:
Hollow core slabs
Prestressed concrete
Concrete damage plasticity
Strengthening
Near surface mounted
CFRP
Openings
Finite element modelling

ABSTRACT

Prestressed Hollow Core Slabs (PHCSs) have become widely used in the construction industry owing to their economic benefits. During their service life, changes that would require openings to be situated along their spans may arise. A strengthening technique to recover or improve the original serviceability and resistances becomes indispensable. Limited research interest has been given to develop appropriate strengthening methods for the PHCSs with openings. The Near Surface Mounted (NSM) strengthening technique is among the practical and feasible solutions to rehabilitate or enhance the performance of these PHCSs. This paper demonstrates a Finite Element (FE) analysis technique to predict the responses of the PHCSs with openings, either unstrengthened or strengthened with NSM strips. The Concrete Damage Plasticity (CDP) model was successfully implemented to model the non-linear behaviour of concrete. The prestressing transmission length and the bond behaviour between the epoxy adhesive and concrete interfaces were put into practice. Acceptable agreements were found, upon validating the FE analysis results against the experimental data available in the literature. Maximum differences, compared to the experimentally attained results in the ultimate loads and the corresponding deformations of nearly 4% and −8.4%, respectively, were detected. An extensive parametric study was executed to assess the effect of various parameters on the overall behaviour of the examined slabs. The PHCS cross-sectional shape, CFRP reinforcement percentage, average precompression, opening location and size and the concrete compressive strength were taken as parameters. Above all, a gap of knowledge exits regarding the presence of design guidelines that evaluate reductions in the ultimate capacities of the PHCSs associated with the presence of openings at multiple locations along their spans and improvements experienced by employing the NSM strengthening technique. This could be bridged by utilizing the suggested modelling approach and the parametric study results in this research.

1. Introduction

PHCSs are precast prestressed concrete elements mostly used in multi-story residential, commercial and industrial buildings. The reduced own weight of the slabs attributed to the presence of the cores makes the cross-section more efficient in resisting the acting straining actions. The slabs are produced on casting beds by the extrusion process, where a zero slump concrete mix is used. This facilitates that the slab preserves its shape after extrusion. Subsequently, the PHCSs are cured under appropriate temperature and moisture conditions. Upon reaching the required strength, the prestressing strands can be released, and the slabs are cut according to the required length.

Openings are probable to be needed in an existing structure to allow the installation of an equipment or the passage of facilities ducts. Structural openings experiencing the cutting of the prestressing strands in the PHCSs, cause a disturbed region having a non-linear distribution of stresses. This effect is reduced gradually in a distance equal to the depth of the member away from the point of occurrence of the disturbance, according to Saint-Venant's principle. This disturbance can cause a severe reduction in both the stiffness and strength of the PHCSs [1].

Due to the mentioned manufacturing process, the reinforcement provided in this type of slabs is exclusive to the prestressing strands, and it is impractical to introduce any additional nonprestressed steel reinforcement to compensate for the depletion in the concrete cross-sectional area and the prestressing steel reinforcement loss. Therefore, it becomes crucial to strengthen the slabs to restore the original capacity

* Corresponding author.
E-mail addresses: Omar.elharouney@eng.asu.edu.eg (O. Elharouney), Mahmoud.elkateb@eng.asu.edu.eg (M. Elkateb), Ayman.hussein.khalil@eng.asu.edu.eg (A. Khalil).

https://doi.org/10.1016/j.engstruct.2021.112262

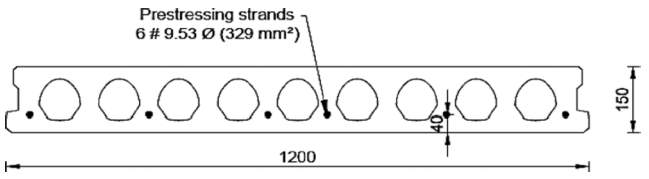

Fig. 1. Cross-sectional details of the PHCSs tested, Pachalla et al. [1].

with a sort of external reinforcement.

Strengthening concrete structures with Fiber Reinforced Polymers (FRP) offers a giant leap forward with respect to other available techniques of strengthening including concrete jacketing and steel plates attachment due to their exceptional mechanical properties, ease of application, low weight and durability [2].

Two techniques are available for strengthening using FRP materials: externally bonded (EB) and NSM techniques. The NSM technique has many advantages, compared to the EB technique, encompassing the less exposure to the environmental conditions leading to better FRP protection. The better debonding resistance and the reduced surface preparation required for installation are among the extra benefits achieved.

The choice of the Carbon Fiber Reinforced Polymers (CFRP) for the PHCSs strengthening is attributed to the superior mechanical properties, compared to other FRP types, which makes the required FRP area less, thus a smaller groove size.

Compared to the strengthening of other concrete elements, a limitation exists in the case of the strengthening of the PHCSs. The longitudinal voids of the PHCSs constrain the positioning of the CFRP reinforcement and make it limited to be at the locations of the webs, due to the smaller thicknesses of the PHCSs' flanges.

Suffice it to say, there is a lack of studies that explain how the FRP strengthened PHCSs without openings behave [3,4]. Elgabbas et al. [3] performed experimental and analytical investigations on the structural behaviour of the PHCSs strengthened with EB and NSM CFRP laminates. A capacity enhancement reaching 80% was recorded at a similar deformability to the control PHCS for the NSM strengthened specimens, while a severely reduced deformability for the EB strengthened PHCSs was evidenced. Generally, it was observed that the strengthened PHCSs had a better distribution of cracks in contrast to the unstrengthened ones.

Foubert et al. [4] tested up to failure a set of NSM strengthened PHCSs, in which both the flexural and shear capacities were magnified. Unexpectedly, the deflection ductility of the PHCSs increased by the attachment of the NSM strips, while the cracking loads were nearly unvaried.

Nonetheless, there is a dearth of experimental [5] and FE studies that handle the PHCSs with openings, especially the ones strengthened with NSM CFRP strips. That is why the authors were motivated to conduct this study. Mahmoud et al. [5], after conducting an experimental testing of a group of PHCSs with NSM CFRP strengthened openings, concluded that the authors' suggested strengthening scheme restored the capacities of the initial PHCSs; besides, extra strengths were further achieved.

This paper presents an approach for the FE modelling of the PHCSs in which openings are provided, with/without NSM CFRP strengthening, using ABAQUS. Firstly, FE models were constructed for experimentally tested PHCSs by Pachalla et al. [1] and Mahmoud et al. [5]. The reliability of the FE models was verified by comparing the numerically predicted results with the experimental results reported, and reasonable accuracy was achieved. Additionally, a parametric study including the effects of diverse factors affecting the ultimate load-carrying capacities of the studied PHCSs was performed, whose results could possibly help in reaching a better understanding of the way of behaving of the PHCSs

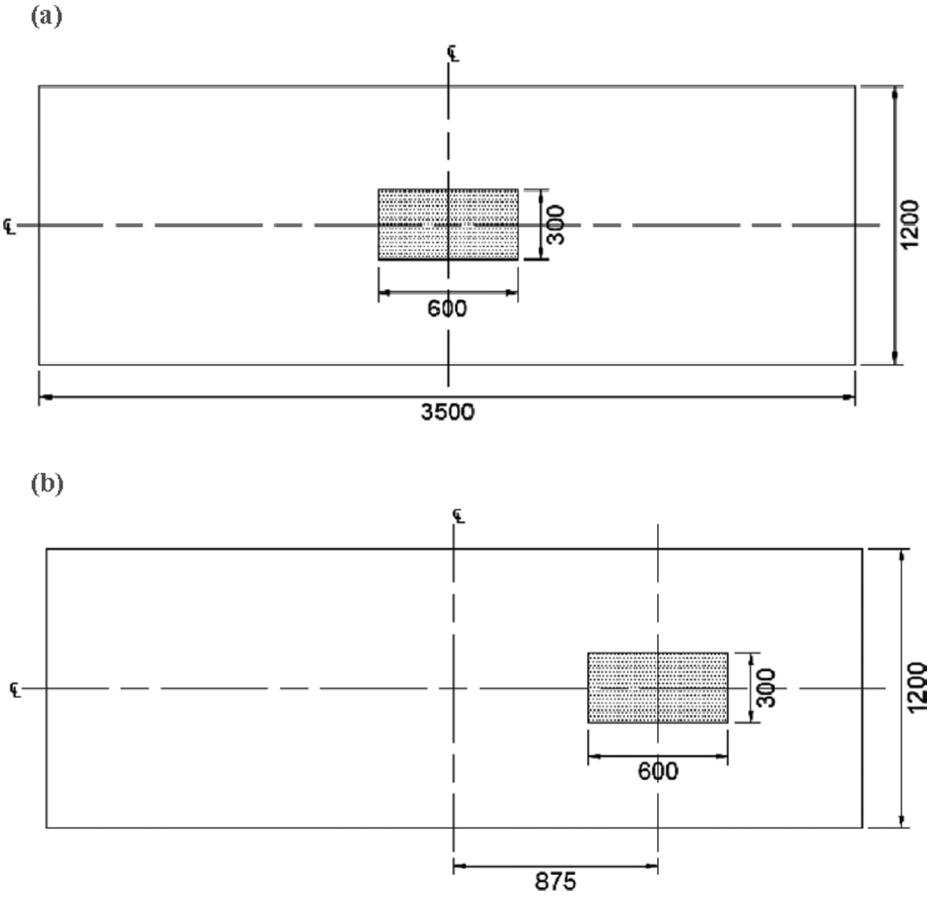

Fig. 2. Plan views for the PHCSs tested by Pachalla et al. [1]: (a) Specimens with a flexural span opening and (b) Specimens with a shear span opening.

Table 1
Test matrix for the specimens tested, Pachalla et al. [1].

Specimen number	Label	a/d	Location of opening
1	HCS-150–3.50-NO	3.5	No opening
2	HCS-150–3.50-FO	3.5	Flexural span
3	HCS-150–3.50-SO	3.5	Shear span
4	HCS-150–7.50-NO	7.5	No opening
5	HCS-150–7.50-FO	7.5	Flexural span
6	HCS-150–7.50-SO	7.5	Shear span

Table 2
Summary of the details of the specimens tested, Mahmoud et al. [5].

Specimen	Concrete compressive strength, MPa	Location of opening	Strengthening
NO-O	64	No opening	N/A
FO-O	64	Flexural span	N/A
FO-S	56.5	Flexural span	Strengthened with NSM strips
SO-O	56.5	Shear span	N/A
SO-S	56.5	Shear span	Strengthened with NSM strips

examined.

2. Experimental program overview

Pachalla et al. [1] studied the effect of openings on the behaviour of PHCSs through the experimental testing of six full-scale specimens. The concrete used to cast the slabs had a cylindrical compressive strength of 34 MPa. The slabs had six seven-wire low-relaxation prestressing strands with a diameter of 9.53 mm, each of which was jacked with a prestressing force of 70 kN. The strands had an ultimate tensile strength of 1860 MPa. The PHCSs were 3500 mm long with a depth and width of 150 mm and 1200 mm, respectively for each specimen. Fig. 1 shows the cross-sectional details of the PHCSs tested. The parameters selected were the shear span to depth ratio a/d and the location of openings. Two a/d values of 3.5 and 7.5 were chosen and the opening could be at the mid-span or within the shear span. Fig. 2 displays a plan view for the specimens with the locations of openings indicated. Table 1 summarizes the text matrix.

Moreover, five full-scale PHCSs were constructed and tested by Mahmoud et al. [5]; all the slabs were 203 mm deep, 1216 mm wide and 5000 mm long. The PHCSs were cast with high strength concrete; the compressive strength of each PHCS is shown in Table 2. The slabs had a prestressing reinforcement of seven size 9 strands. The strands were seven-wire low-relaxation steel strands of grade 1860. The jacking stress was 0.75 of the tensile strength of the prestressing steel strands. The first slab acted as a control specimen without openings. Two of the tested slabs had an opening at the mid-span, while the other two had an opening within the shear span. The exact locations of the openings are shown in Fig. 3. For each opening location, one slab acted as a reference, while the other was strengthened with NSM CFRP strips. The openings were cut after the slabs were cast. The openings had dimensions of 308 mm wide and 600 mm long [5]. Table 2 summarizes the examined specimens details.

The CFRP strips used were of 2 mm thickness and 16 mm in width. The modulus of elasticity and tensile strength of the strips are 131 GPa and 2068 MPa, respectively, according to standard tests executed by the supplier. The strengthened slabs had two longitudinal strips, that were discontinued at a distance of 200 mm from the supports, and four transverse strips of lengths of 1008 mm. The strips were attached to the

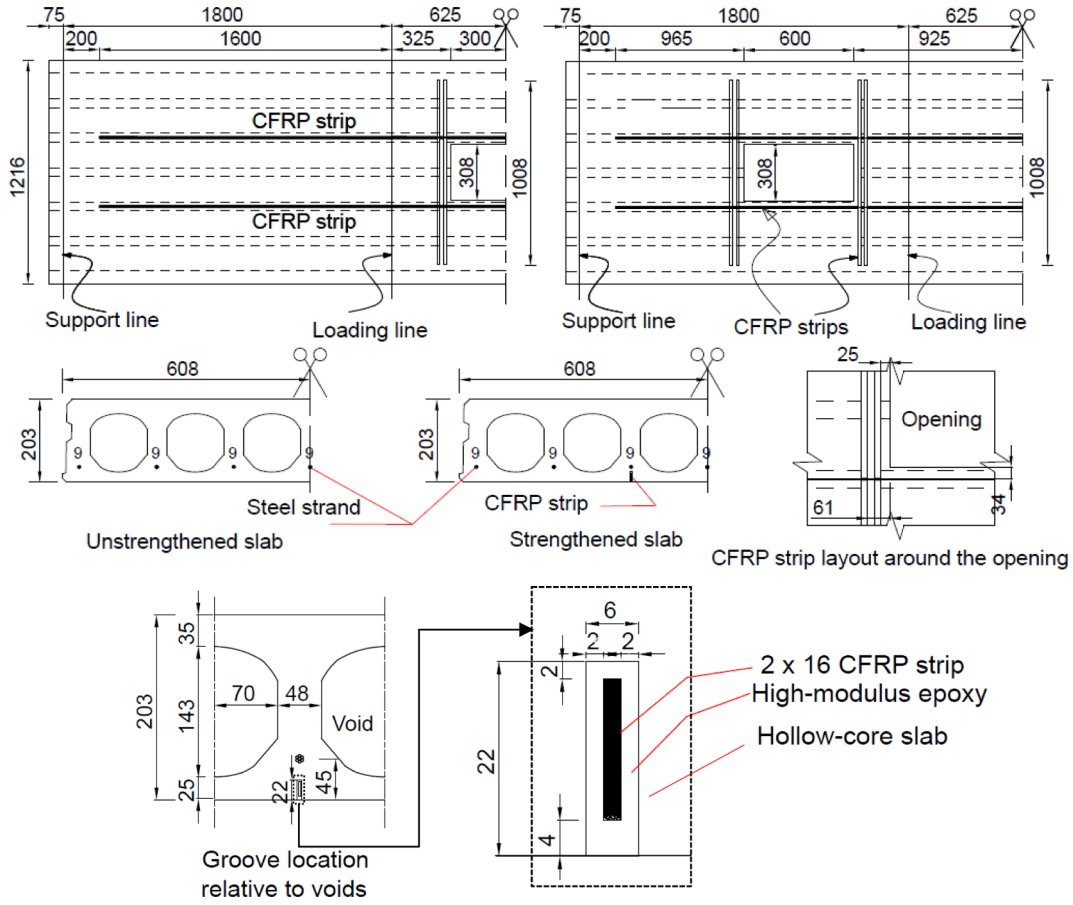

Fig. 3. Detailed plans and cross-sections for the experimentally tested specimens, Mahmoud et al. [5].

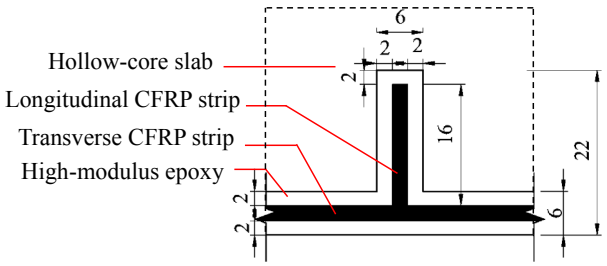

Fig. 4. Cross-section at the strips intersection around the openings, Mahmoud et al. [5].

PHCSs by means of an epoxy adhesive having a modulus of elasticity of 3792 MPa and tensile strength of 62 MPa [5]. Fig. 3 indicates the geometrical details of the tested slabs and the strengthening layout. To avoid the interference of the longitudinal and transverse strips at their intersections, the orientation of the transverse strips was changed and could not be the same as the longitudinal strips. Fig. 4 displays the strips intersection detail around the openings.

3. Finite element analysis

3.1. Finite element model

Three-dimensional non-linear FE models, for specimens 1 and 2 examined by Pachalla et al. [1] and the five tested PHCSs by Mahmoud et al. [5], were constructed using the ABAQUS FE software package. A multi-step static analysis was performed in this study. The purpose of the first loading step was to transfer the prestressing forces from the strands to the surrounding concrete simulating the strands detensioning causing a camber along the length of the slab.

The prestressing effect was modelled through assigning initial stresses to the strands, taking into consideration the prestressing losses occurring. It should be noted that the transmission lengths for the prestressing strands were calculated according to Eurocode 2 (2004) [6] provisions. The realistic simulation of the transmission length of the prestressing is vital for the PHCSs, as it has a direct effect on the prestressing force value affecting the cross-section of the concrete. The stress in a strand should be equal to zero at the ends of the PHCS, and it was assumed to vary linearly from the end and across the transmission length.

Furthermore, the inclusion of an opening at the location of the strands in a PHCS would change the distribution of the prestressing forces in the cut strands. The opening was pre-cut within the FE simulation at the initiation of the analysis, however to consider the above-mentioned change, an assumption was made that the prestressing forces in the cut strands would be reduced to zero at the opening edges and to increase linearly across the transmission length of prestressing. On the contrary, for the strands adjacent to the opening, the forces due to prestressing were presumed to be unaltered.

The second step involved the application of displacement boundary conditions to the loading plates to emulate the experimental displacement control loading. The procedures followed to construct the FE models are described in detail. This includes the material models for each element, the interactions between them and the types of mesh elements used to simulate different components of the PHCSs' FE models.

3.2. Modelling of materials

3.2.1. Concrete constitutive model

The CDP model [7] was used to model the behaviour of the concrete in this study. It is based on the continuum damage plasticity assuming the compressive crushing and tensile cracking of concrete as the major failure mechanisms. The basis of the yield criterion of this constitutive

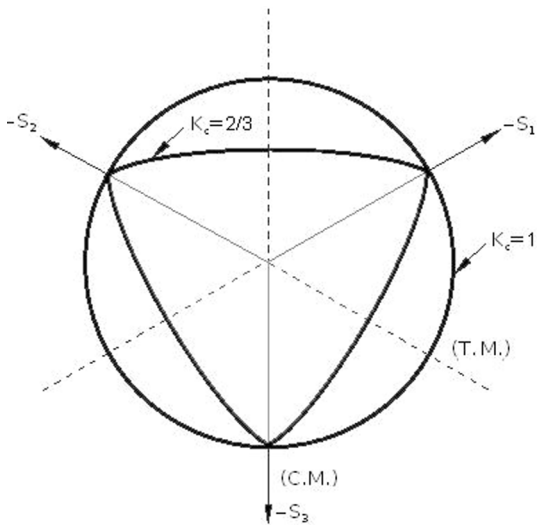

Fig. 5. Failure surface in the deviatoric plane in the CDP model, Hibbit et al. [7].

Table 3
Summary of the parameters of the CDP model.

Parameter	Value
Dilation angle (φ)	36°
Eccentricity (m)	0.1
Ratio of initial equi-biaxial compressive yield stress to initial uniaxial compressive yield stress (f_{bo}/f_c)	1.16
Ratio of the second stress invariant on the tensile meridian to the compressive meridian ($\rho_t / \rho_c = K_c$)	2/3
Viscosity parameter (μ)	0.0001

model is the Drucker-Prager criteria, yet incorporating the modifications suggested by Lubliner et al. [8] and Lee and Fenves [9]. Upon which, it has been supposed that the failure surface in the deviatoric plane may not have a circular shape, and the parameter K_c was introduced to describe this modification, as shown in Fig. 5, where K_c is the ratio between the second stress invariant on the tensile meridian and that on the compressive meridian.

To entirely define the plastic behaviour of concrete, four additional parameters, namely φ, m, f_{bo}/f_c and μ, have to be determined. In addition, the uniaxial stress–strain relationship of concrete has to be described. The dilation angle φ can be physically demonstrated as the concrete internal friction angle. Recognizing that the FE models' results are highly sensitive to the value of φ, four values of 28°, 32°, 36° and 40° were chosen to study its effect on the load–deflection behaviour. A dilation angle of 36° succeeded in reaching a best-fit to the experimental results.

The plastic potential eccentricity m can be quantified as the ratio of the tensile to the compressive strength of concrete. Relying on the ABAQUS's recommendations, a value of 0.1 was assigned for m to evade the convergence difficulties when low confining pressures are affecting the concrete. The ratio of the initial equi-biaxial compressive yield stress to the corresponding uniaxial compressive yield stress f_{bo}/f_c can relate the concrete strength under biaxial loading to that under uniaxial compression. The values of 2/3 and 1.16 for K_c and f_{bo}/f_c, respectively, were adopted in this study, which are the ABAQUS's default values.

To overcome the convergence difficulties during a static analysis, due to the stiffness degradation and the geometrical discontinuity in the case of the PHCSs with openings, in particular, a value of 0.0001 was used for the viscosity parameter μ. This permits the concrete material to surpass the plastic potential surface, thus increasing the stability, yet without a noticeable effect on the results, as will be shown in Section 4.

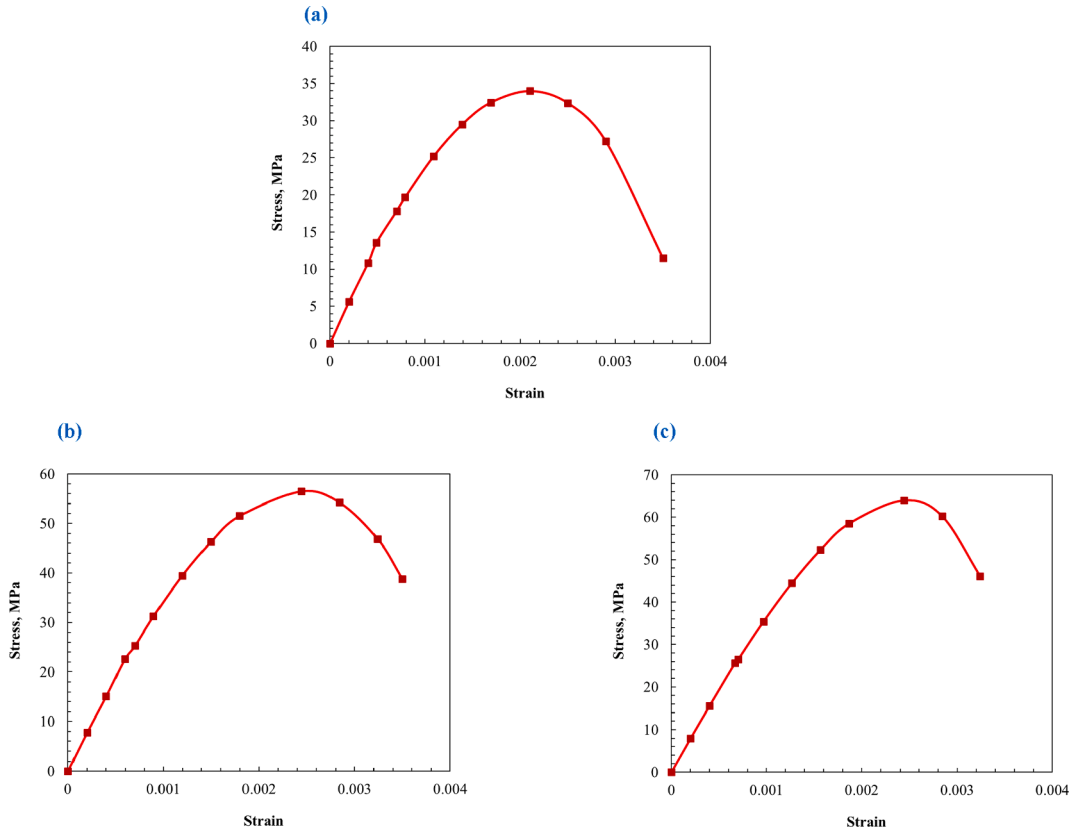

Fig. 6. (a) Stress–strain curve for uniaxial compression for specimens HCS-150–3.50-NO and HCS-150–3.50-FO, (b) Stress–strain curve for uniaxial compression for specimens FO-S, SO-O and SO-S and (c) Stress–strain curve for uniaxial compression for specimens NO-O and FO-O.

Table 3 gives the parameters of the CDP model used in this study.

The uniaxial stress–strain relationship of concrete, after being transformed to stress versus inelastic strain by using **Eqs. 1** and **2**, is converted to a stress-plastic strain curve by ABAQUS.

$$\varepsilon_c^{in} = \varepsilon_c - \varepsilon_c^{el} \tag{1}$$

with

$$\varepsilon_c^{el} = \frac{\sigma_c}{E_0}$$

where ε_c is the strain in the concrete at a given stress σ_c, ε_c^{el} is the concrete elastic strain, ε_c^{in} is the concrete inelastic strain and E_0 is the concrete modulus of elasticity.

3.2.1.1. Stress–strain curve for uniaxial compression. The uniaxial compressive stress–strain of concrete material was determined as an elastic–plastic behaviour conforming with Eurocode 2 (2004) [6] that is defined by **Eqs. (3–8)**.

$$\frac{\sigma_c}{\sigma_{cu}} = \frac{k\eta - \eta^2}{1 + (K-2)\eta} \tag{3}$$

$$\eta = \varepsilon_c/\varepsilon_{c1} \tag{4}$$

$$\varepsilon_{c1} = 0.7{\sigma_{cu}}^{0.31} \tag{5}$$

$$\varepsilon_{cu1} = 2.8 + 27[0.01(98 - \sigma_{cu})]^4 \tag{6}$$

$$k = 1.05E_{cm}|\varepsilon_{c1}|/\sigma_{cu} \tag{7}$$

$$E_{cm} = 22\left(\frac{\sigma_{cu}}{10}\right)^{0.3} \tag{8}$$

where ε_{c1} is the strain value at the maximum compressive stress σ_{cu}, ε_{cu1} is the concrete compressive strain at failure and E_{cm} is the secant modulus of elasticity of concrete between $\sigma_c = 0$ and$\sigma_c = 0.4\sigma_{cu}$. Fig. 6 shows the uniaxial stress–strain curves in compression that have been input in ABAQUS for the modelled specimens.

3.2.1.2. Stress–strain curve for uniaxial tension. The tensile behaviour of concrete is assumed to be linearly elastic up to the maximum tensile stress with the concrete elastic modulus, before the onset of cracking, which is followed by a non-linear softening response, that was necessary to be described so as to take into account the tension stiffening phenomenon. Eurocode 2 (2004) [6] evaluates the tensile strength of concrete σ_{t0} for concrete compressive strengths higher than 50 MPa according to **Eq. (9)**, that was implemented in this study for the examined specimens by Mahmoud et al. [5]. For the specimens tested by Pachalla et al. [1], a value of 2.4 MPa was taken for the tensile strength of concrete as reported by the authors.

$$\sigma_{t0} = 2.12ln\left(1 + \left(\frac{\sigma_{cu}}{10}\right)\right) \tag{9}$$

Tamai et al. [10] proposed **Eq. (10)** to describe the non-linear descending branch of the stress–strain curve, where a power constant of 0.4 yielded the best fit to the experimental stress–strain curves investigated. As the tension stiffening effect depends on multiple factors and has a crucial effect on the analysis results, Kmiecik et al. [11] suggested a modification to **Eq. (10)** in order to allow calibration during the FE models refining by introducing a new variable n instead of the power constant previously suggested by Tamai et al. [10]. **Eq. 11** describes the modified equation that was utilized in this study.

$$\sigma_t = \sigma_{t0}\left(\frac{\varepsilon_{cr}}{\varepsilon_t}\right)^{0.4} for \varepsilon_t > \varepsilon_{cr} \tag{10}$$

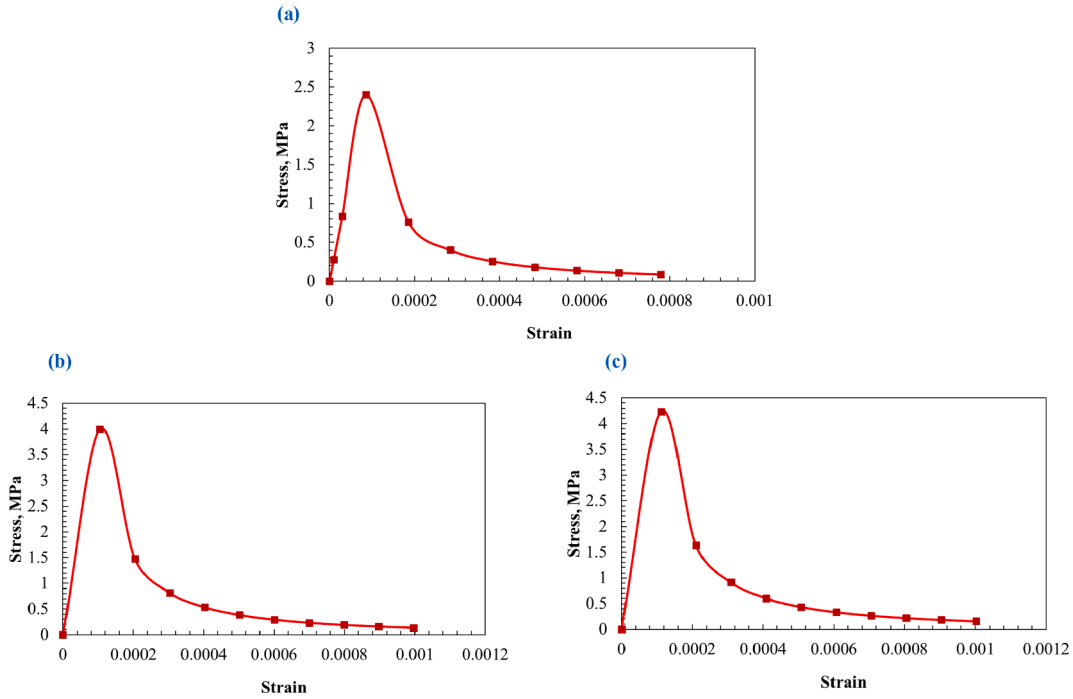

Fig. 7. (a) Stress–strain curve for uniaxial tension for specimens HCS-150–3.50-NO and HCS-150–3.50-FO, (b) Stress–strain curve for uniaxial tension for specimens FO-S, SO-O and SO-S and (c) Stress–strain curve for uniaxial tension for specimens NO-O and FO-O.

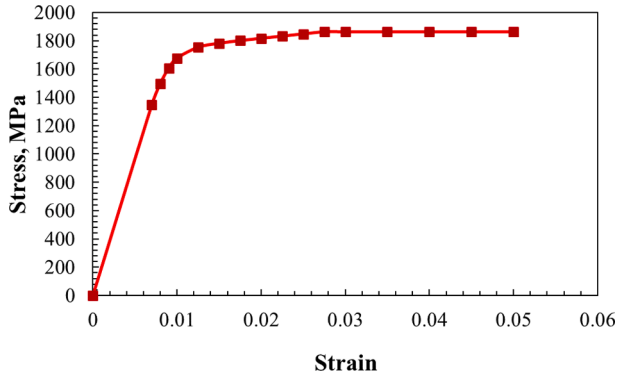

Fig. 8. Stress–strain curve of prestressing steel.

$\sigma_t = \sigma_{t0}\left(\frac{\varepsilon_{cr}}{\varepsilon_t}\right)^n$ for $\varepsilon_t > \varepsilon_{cr}$ *(11)*where ε_t is the concrete tensile strain at given stressσ_t, ε_{cr} is the concrete tensile strain at cracking and n represents the rate of weakening of the post-peak behaviour.

It should be emphasized that for prestressed concrete elements, and particularly for the PHCSs, in which no other type of reinforcement rather than the prestressing strands exists, the tension stiffening effect becomes less evident.

Also, as the value of *n* increases, the rate of decay of the tensile stress increases signifying less tension stiffening. Having conducted an iterative calibration approach for different values of *n*, a value of 1.5 was taken in this study. See Fig. 7 for the uniaxial tensile stress–strain curves defined in ABAQUS for the analysed PHCSs.

3.2.2. *Prestressing steel reinforcement*

A non-linear elastoplastic model, that follows the stress–strain relation developed by Devalapura et al. [12] for seven-wire low-relaxation strands, was used for modelling the strands material tensile behaviour in this study. This empirical relationship, described in **Eq. (12)**, is a further refinement of the formula originally presented by Skogman et al. [13].

Table 4
Power formula constants for grade 1860 strands, Devalapura et al. [12].

Strand type	f_{py}/f_{pu}	A	B	C	D
Grade 1860	0.90	887	27,613	112.4	7.360

f_{py} is the yield strength of the prestressing strands.

Besides, the initial elastic modulus and Poisson's ratio were taken as 197 GPa and 0.3, respectively. Fig. 8 shows the obtained stress–strain response of the prestressing strands in this study.

$$f_{ps} = \varepsilon_{ps}\left[A + \frac{B}{\left\{1 + \left(C\varepsilon_{ps}\right)^D\right\}^{\frac{1}{D}}}\right] \leq f_{pu} \tag{12}$$

where f_{ps} is the stress corresponding to a given strain ε_{ps} and f_{pu} is the ultimate strength under tension of the prestressing strands. Additionally, A, B, C and D are constants determined from Table 4 for grade 1860 strands modelled in this study.

3.2.3. *CFRP strips, epoxy adhesive, loading and support plates*

The tensile behaviour of the CFRP strips was assumed to be linear up to the ultimate tensile strength, as shown in Fig. 9 **(a)**. Fig. 9 **(b)** shows the bi-linear elastic stress–strain curve assigned to the epoxy adhesive. The stress–strain responses are based on the manufacturer tests, as reported by Mahmoud et al. [5].

A linear elastic material was assigned to both the steel loading and support plates with a modulus of elasticity of 200 GPa and a Poisson's ratio of 0.3.

3.3. *Mesh elements*

The concrete, epoxy adhesive, loading and supporting plates were simulated using an element type called C3D8R. It is a three-dimensional solid element that can take into account both the linear elastic or non-linear elastoplastic characteristics of materials. The prestressing strands and the CFRP strips were modelled using an element type called

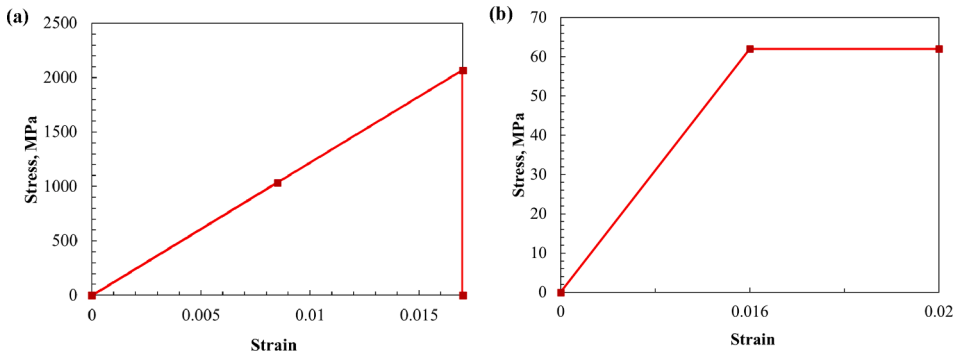

Fig. 9. Stress–strain curves: (a) CFRP strips and (b) Epoxy adhesive.

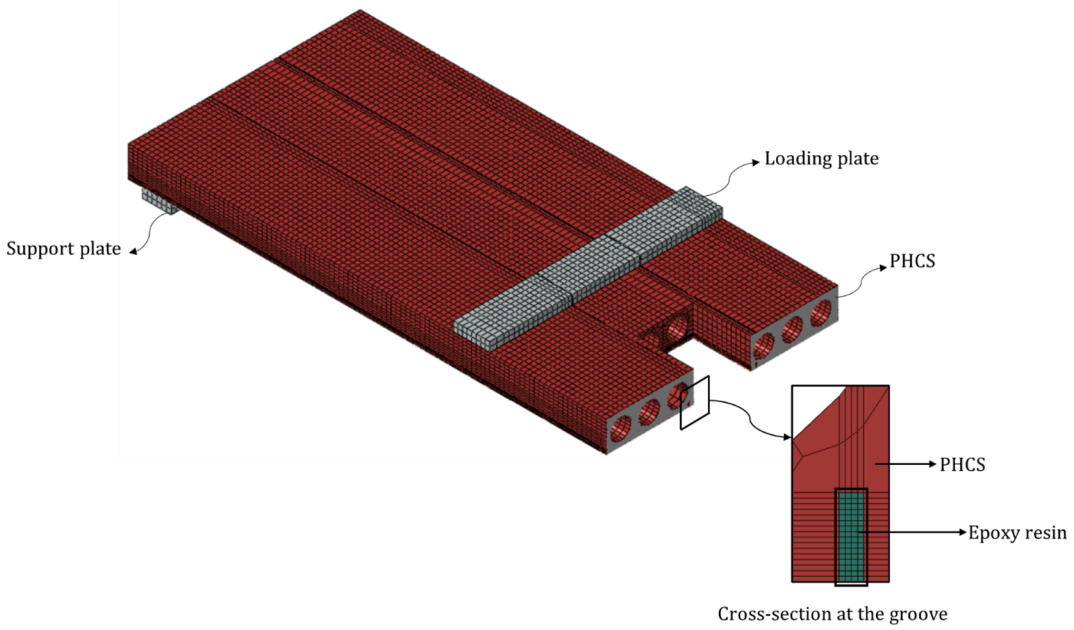

Fig. 10. 3D meshing of the PHCS in the FE model.

T3D2. It is a 2-node linear 3D truss element that is capable of resisting axial compression and tension forces.

Mesh sensitivity analysis for the determination of an optimum mesh size was performed, where an element of size 25 mm was chosen. However, a finer mesh was defined at the grooves for the strengthened PHCSs to visualise a more accurate debonding behaviour at the epoxy-concrete interface. Fig. 10 introduces the meshed PHCS in the FE model.

3.4. Interactions between the FE models' components

The prestressing strands were considered to be perfectly bonded to the concrete, which may be an acceptable simplification, in addition that modelling the bond-slip behaviour between the strands and the concrete would dramatically increase the computational cost of the FE model. An embedded region constraint was made use of to model the concrete-strand interaction. This constraint allows embedding of a region of the model, which was the prestressing strands, within a host region of the model, which was the concrete.

A surface-based tie constraint was used to define the interaction between the loading and support plates, and the concrete. An in-depth illustration of the interaction between the CFRP strips and the concrete highly demands attention, which will be introduced in the following subsection.

3.4.1. The bond between the CFRP strips and the concrete substrate

To ensure that the behaviour of the strengthened PHCSs was realistically simulated, the bond-slip interaction between the CFRP strips and the concrete substrate was implemented in the proposed model. It is well recognized that the epoxy-concrete interface is the weakest interface along which the debonding failure would most probably occur [14,15]; this also conforms with the debonding mode of failure visualised by Mahmoud et al [5] in the experimental testing. On these grounds, a perfect adhesion behaviour was supposed for the interaction between the CFRP and epoxy adhesive in the FE models, while a thorough representation of the debonding reponse at the epoxy-concrete interface was of much importance.

Though the epoxy-concrete interface is subject to both normal and shear stresses yielding a mixed-mode failure, the majority of earlier studies analysed the debonding behaviour on the basis of a shear stress-slip model only. In this study, a surface-based cohesive interaction was assigned to the epoxy-concrete interface allowing the mixed-mode debonding to take place by employing a normal traction-separation law side by side with a tangential traction-separation law.

The damage initiation at the interface was said to be triggered when a quadratic interaction equation, defined in ABAQUS, comprising the maximum nominal stress ratios reached the value of one, according to **Eq. (13)** [7].

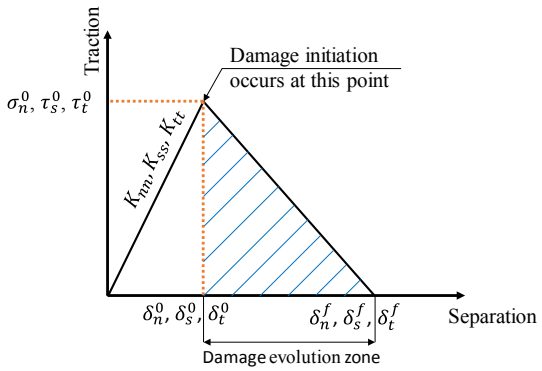

Fig. 11. Schematic representation of the tangential and normal traction-separation behaviours.

$$\left\{\frac{\sigma_n}{\sigma_n^0}\right\}^2 + \left\{\frac{\tau_s}{\tau_s^0}\right\}^2 + \left\{\frac{\tau_t}{\tau_t^0}\right\}^2 = 1 \tag{13}$$

where σ_n,τ_s and τ_t represent the acting contact stresses in a direction normal to the interface or in the first or second shear directions, respectively,σ_n^0,τ_s^0 and τ_t^0 represent the maximum values of the contact stress when the separation is in a direction normal to the interface or in the first or second shear directions, respectively, and δ_n^0, δ_s^0 and δ_t^0 designate the corresponding separations, respectively.

After the initiation of the damage takes place, a gradual degradation of the stiffness of the interface, denoted as damage evolution, arises. It could be defined in terms of the fracture energy released until the full degradation of the stiffness.

A schematic representation of the traction-separation behaviour is demonstrated in Fig. 11, where K_{nn}, K_{ss} and K_{tt} stand for the normal and the shear stiffness in both directions of the interface, respectively, and δ_n^f, δ_s^f and δ_t^fidentify the separations at the full debonding in the normal direction to the interface or in the first or second shear directions, respectively. Benzeggagh-Kenane fracture criterion was utilized in this research to specify the mixed-mode behaviour in ABAQUS [16].

The bond failure could be tracked in ABAQUS through the output of two variables that take values from zero to one namely; the quadratic stress-based damage initiation criterion CSQUADSCRT and the damage variable for cohesive surfaces CSDMG. Damage in ABAQUS was considered to be initiated and full debonding was regarded to take place when the value of the first and the second reached one, respectively.

The models describing the tangential and normal traction-separation behaviours are illustrated in the next subsections.

3.4.1.1. Shear stress-slip model. The shear stress-slip model proposed by Zhang et al. [17] was considered in this study to compute the maximum shear stress components. **Eq. 14** describes the mathematical relationship to predict the maximum shear contact stresses τ_s^0 and τ_t^0 [17].

$$\tau_s^0 = \tau_t^0 = 1.15\gamma^{0.138}\sigma_{cu}^{0.613}$$

where γ is the groove height to width ratio.

The separations at the full debonding stage δ_s^f and δ_t^f were attained by **Eq. 15** according to the fracture energy of the epoxy-concrete interfaceG_{FI}, as described by **Eq. (16)** suggested by Zhang et al. [17], and the maximum bond stress at the interface recalling that the interface fracture energy is equal to the area under the shear stress-slip model.

$$\delta_s^f = \delta_t^f = 0.696\gamma^{0.284}\sigma_{cu}^{0.006}$$

$$G_{FI} = 0.4\gamma^{0.422}\sigma_{cu}^{0.619} \tag{16}$$

3.4.1.2. Normal stress-gap model. The normal stress and fracture energy of the epoxy-concrete interface were restricted to the tensile strength and fracture energy of the concrete, respectively [18,19]. The equation proposed by CEB-FIP Model Code 1990 [20] **Eq. (17),** was used to predict the fracture energy of concreteG_{FC}. From **Eqs. (9) and (17),** the contact gap at the full debonding stage could be calculated, as described by **Eq. (18),** taking into consideration the assumption that the area under the normal stress-gap model represents the concrete fracture energy.

$$G_{FC} = G_{Fo}\left(\frac{\sigma_{cu}}{10}\right)^{0.7} \tag{17}$$

where G_{Fo} is the base value of the fracture energy of concrete, that is defined according to the maximum aggregate size.

$$\delta_{nf} = \frac{G_{Fo}\sigma_{cu}^{0.7}}{5.31ln\left(1+\frac{\sigma_{cu}}{10}\right)} \tag{18}$$

4. Finite element results and comparisons

In this section, following the creation of seven FE models for specimens tested by Pachalla et al. [1] and Mahmoud et al. [5], comparisons of the FE results and the experimental data for the tested PHCSs were made to verify the accuracy of the FE modelling technique in this study. In-detail comparisons were held in terms of the load–deflection curves, crack patterns and failure modes.

At the cracking stage, a relatively higher variation percentage between the FE models and test results, compared to the ultimate stage, was observed with a maximum deviation of + 16.3% and + 16% for the cracking loads and displacements, respectively. It was hypothesized to occur because the experimentally tested specimens should always have some sort of cracks before the experimental loading.

It is also noteworthy to mention that the analysis was terminated at the occurrence of failure for all of the validated specimens, except for specimen SO-S where severe convergence difficulties were noticed after the initiation of the debonding failure.The failure was distinguished in the FE models by keeping an eye on the strain values in the concrete, prestressing steel, epoxy adhesive and CFRP strips. Besides, the output variables CSQUADSCRT and CSDMG, formerly illustrated in Section 3.4.1, were traced to identify the CFRP strips debonding failure.

The modes of failure predicted from the FE models well resembled that of the experimental results, which were britlle shear and ductile

Table 5
Comparison of test results with the FE models' results, (Specimens experimentally tested by Pachalla et al. [1]).

Specimen	Results	δ_{cr} (mm)	P_{cr} (kN)	δ_u (mm)	P_u (kN)	Mode of failure
HCS-150–3.50-NO	FE	4.7	143.3	22	182.5	CC
	Exp.	4.3	129.6	20.7	180.7	CC
	Variation (%)	+9.3	+10.6	+6.3	+1.0	
HCS-150–3.50-FO	FE	4.78	88.5	58.6	152.7	CC
	Exp.	4.3	80.5	56.5	156.4	CC
	Variation (%)	+11.2	+9.9	+3.7	−2.4	

P_{cr} and δ_{cr} represent the load and corresponding deflection at cracking initiation, P_u is the ultimate load and δ_u is the corresponding deflection and CC = concrete crushing.

Table 6
Comparison of test results with the FE models' results, (Specimens experimentally tested by Mahmoud et al. [5]).

Specimen	Results	δ_{cr} (mm)	P_{cr} (kN)	δ_u (mm)	P_u (kN)	Mode of failure
NO-O	FE	8.70	90	68.2	110	CC & SR
	Exp.	7.5	81	68.5	108	CC & SR
	Variation (%)	+16	+11.1	−0.4	+1.9	
FO-O	FE	8.1	72.7	81.8	95.7	CC & SR
	Exp.	8.2	69	85.4	92	CC & SR
	Variation (%)	−1.2	+5.4	−4.2	+4	
FO-S	FE	9.06	73.67	185.8	130.79	FR & CC
	Exp.	10.1	70	178	129	FR & CC
	Variation (%)	−10.3	+5.2	+4.4	+1.4	
SO-O	FE	7.66	84.9	102.7	106.1	CC & SR
	Exp.	6.8	73	108.6	103	CC & SR
	Variation (%)	+12.7	+16.3	−5.4	+3	
SO-S	FE	7.96	82.8	171.8	135.5	PD
	Exp.	7.1	77	187.6	134	PD & CC
	Variation (%)	+12.1	+7.5	−8.4	+1.1	

P_{cr} and δ_{cr} represent the load and corresponding deflection at cracking initiation, P_u is the ultimate load and δ_u is the corresponding deflection, CC = concrete crushing, SR = strands rupture, FR = FRP strips rupture and PD = premature debonding.

flexural failures for specimens 1 and 2 tested by Pachalla et al. [1], respectively.

The unstrengthened specimens tested by Mahmoud et al. [5] failed due to concrete crushing and prestressing strands rupture. For the strengthened PHCSs, the specimen FO-S failed due to the longitudinal CFRP strips rupture, followed by concrete crushing. For the SO-S specimen, premature debonding of the longitudinal CFRP strips took place accompanied by convergence problems in the FE model, after which the analysis was terminated. Experimentally, after the CFRP strips debonding, a concrete crushing failure was experienced [5].

On the contrary to the cracking phase, at the ultimate stage, the predicted FE models' loads were nearly identical to those of the experimental results with a maximum error percentage of nearly + 4%. Additionally, the highest variation in the corresponding deformations to the ultimate loads was −8.4%. It is to be stated that the predicted deformations at failure for specimens HCS-150–3.50-NO, NO-O and FO-O were noticeably less than the experimental values due to the fact that the FE analysis for each specimen was discontinued once the failure had been initiated due to convergence problems.

Tables 5 and 6 show a tabulated comparison between the test results and the FE models' results. Figs. 12 and 13 show the load versus deflection responses experimentally obtained and that predicted from the FE models for all modelled specimens.

The crack patterns obtained from the experimental tests and the FE models for the PHCSs tested by Mahmoud et al. [5] are compared in Fig. 14. It could be confirmed that the FE models are capable of effectively predicting the cracks' distributions. Be that as it may, to a small extent, some experimental cracks varied in the way that they were not as continuous along the PHCSs as the FE models' cracks. This was supposed to take place due to the perfect bond assumption between the prestressing strands and concrete, which would increasingly disturb the cracking propagation. Even so, the redistribution of the experimental cracks at the vicinity of the NSM CFRP strips was successfully captured by the FE models, as shown in Fig. 14.

In the end, it could be assured that the results of the FE modelling approach, after being validated with experimental results of specimens having different geometrical properties and loading schemes, match the tests' results to a significant extent. Thus, these models could be employed to perform a parametric study with a fine degree of certainty to take into account the influence of divergent factors that could affect the ultimate capacities of the PHCSs under consideration, which would be introduced in the next section.

5. Parametric study

Having calibrated the FE models with the experimental results, they were employed to conduct a parametric study to estimate the effect of various parameters on the behaviour of the PHCSs with openings either unstrengthened or strengthened with NSM CFRP strips. Among the parameters considered were the effect of the opening size and location along the span of the PHCS. Moreover, the average precompression, CFRP reinforcement percentage, PHCS cross-sectional shape and concrete compressive strength were further considered in this study.

In total, fifty FE models were established to attain the goals of the parametric study. Three series of specimens were constructed, each with a different PHCS in geometry. The lengths of all of the modelled PHCSs were 5000 mm with a clear span of 4850 mm. Each of the specimens was subjected to a four-point bending loading under simply supported

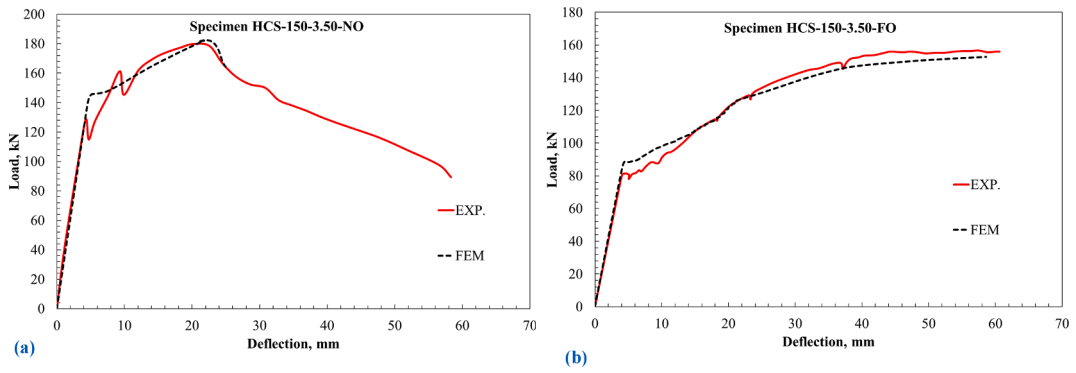

Fig. 12. Comparison between experimental and FE models' results in terms of the load–deflection response: (a) Specimen HCS-150–3.50-NO, (b) Specimen HCS-150–3.50-FO, (Specimens experimentally tested by Pachalla et al. [1]).

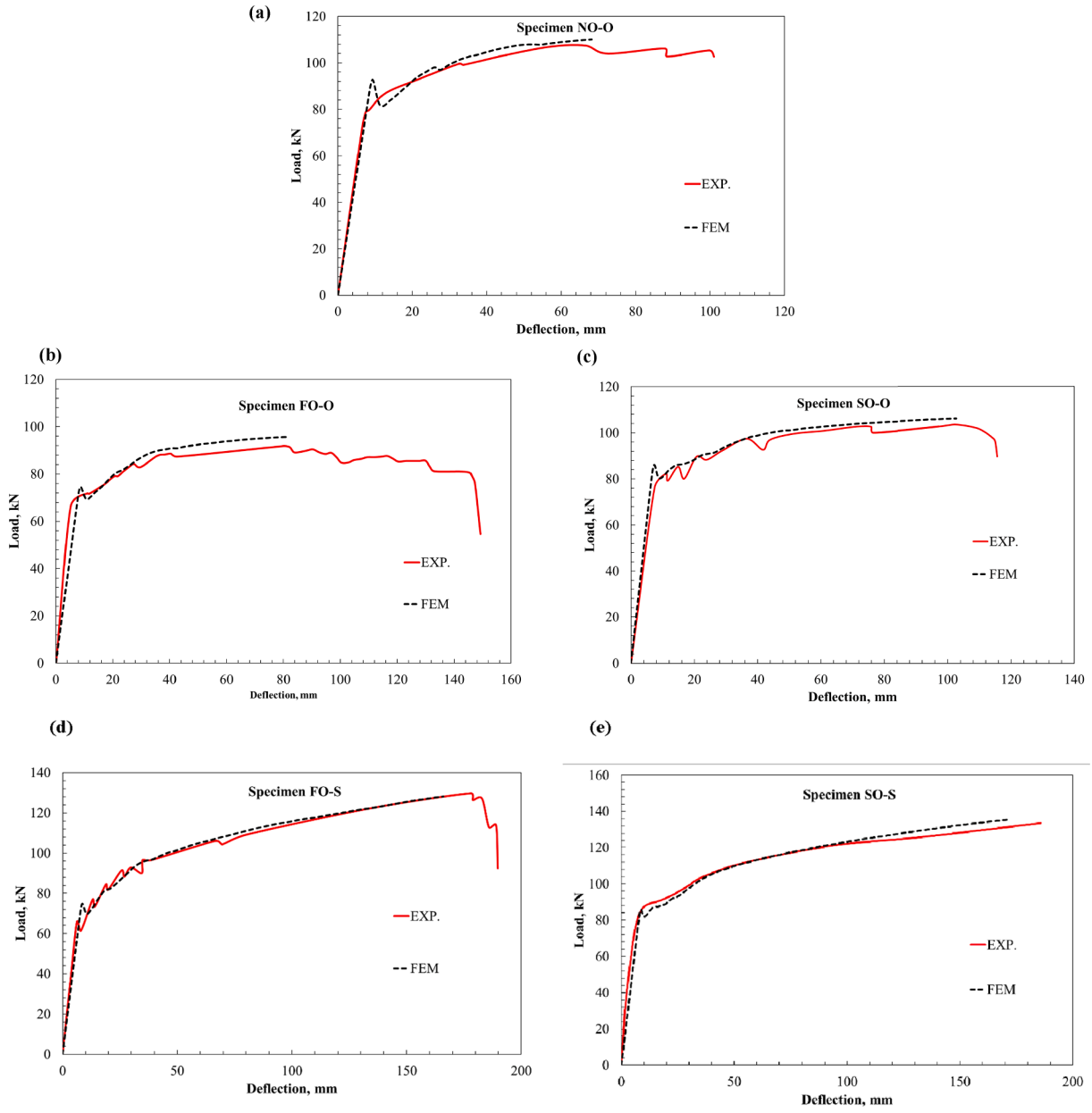

Fig. 13. Comparison between experimental and FE models' results in terms of the load–deflection response: (a) Specimen NO-O, (b) Specimen FO-O, (c) Specimen SO-O, (d) Specimen FO-S and (e) Specimen SO-S, (Specimens experimentally tested by Mahmoud et al. [5]).

conditions with a constant 1800 mm shear span. The prestressing strands were low relaxation strands with an ultimate tensile strength of 1860 MPa and a diameter of 9.3 mm. The concrete compressive strength for all of the modelled specimens was 40 MPa, except for group II (series III), in which a 60 MPa compressive strength concrete was utilized. The exact CFRP strengthening layout employed in the experimental tests by Mahmoud et al. [5] was retained in the parametric study. Fig. 15 shows the loading layout, openings details and strengthening scheme for the modelled PHCSs. In Table 7, a summary of the inspected parameters is presented.

5.1. Series I

A PHCS with a thickness of 160 mm was analysed in this series, whose geometry is shown in Fig. 16. Series I was divided into three groups. Group I was created to provide an interaction between the opening location and size, and the ultimate load-carrying capacity while keeping other parameters unchanged. Groups II and III were formulated to study the influence of the average precompression and CFRP reinforcement percentages.

5.1.1. Group I

A total of 17 FE models were constructed to realize the purpose of group I, in which four prestressing strands were provided yielding an average precompression of 2.11 MPa. The PHCSs with openings in group I were strengthened with a CFRP reinforcement percentage of 0.0581%. The openings dimensions chosen were 300 × 600 mm and 600 × 600 mm, which caused the curtailment of two prestressing strands for both sizes. The opening location was varied along the PHCS length, where the x/s ratio was changed from 0.2 to 0.5 at increments of 0.1. Table 8 summarizes the details of the specimens of group I.

The FE models showed that the effect of the openings on the ultimate loads was more adverse as the openings approached the midspan of the PHCSs, where the reduction reached 49% for an opening of size 600 ×

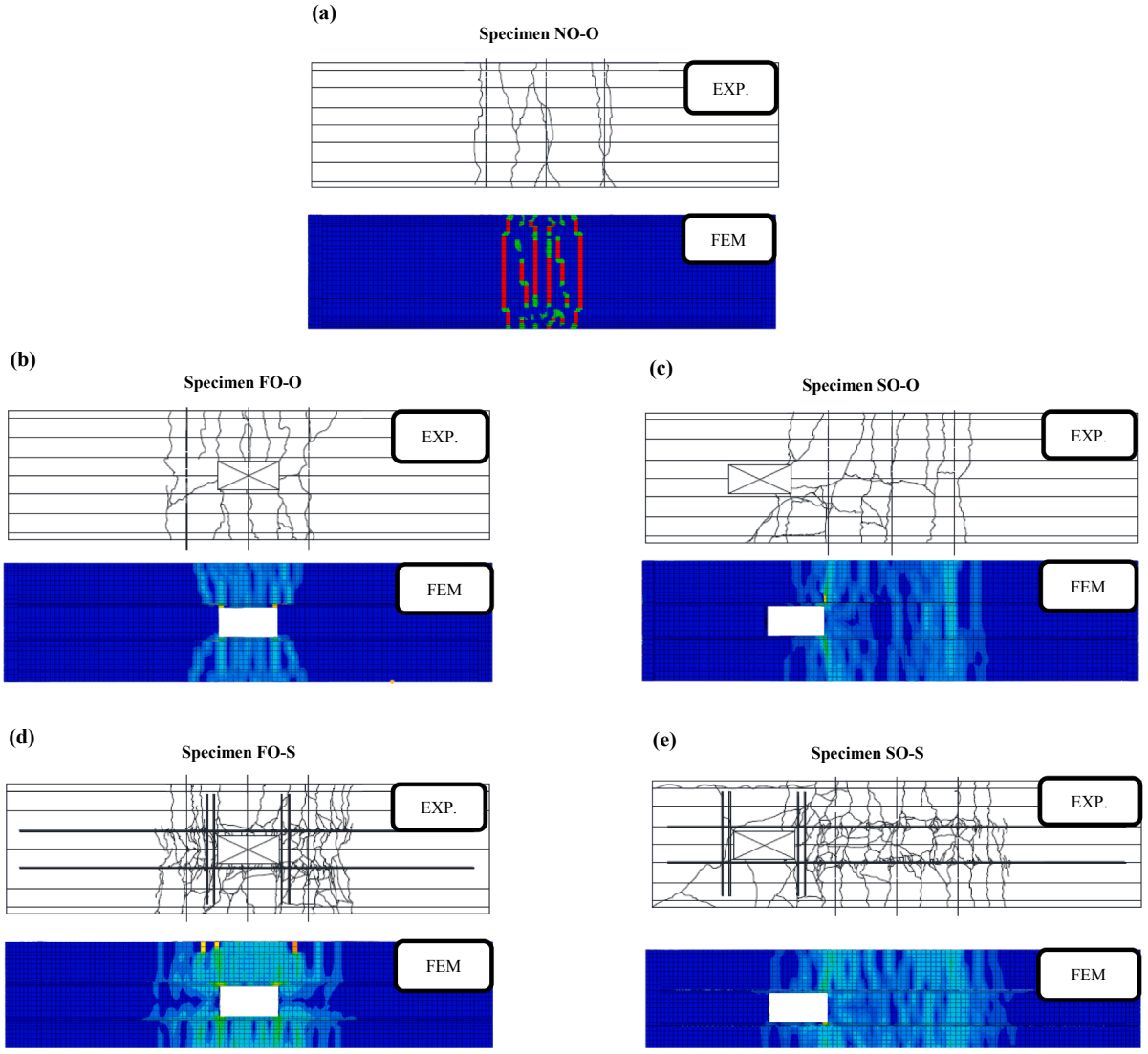

Fig. 14. Comparison of crack patterns between experimental and FE models' results: (a) Specimen NO-O, (b) Specimen FO-O, (c) Specimen SO-O, (d) Specimen FO-S and (e) Specimen SO-S, (Specimens experimentally tested by Mahmoud et al. [5]).

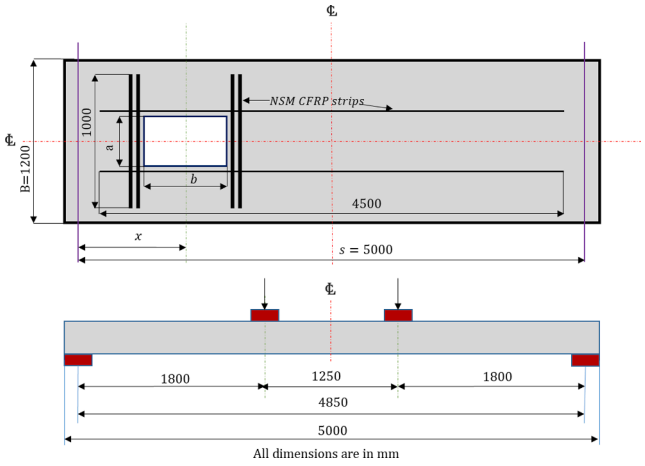

Fig. 15. Plan and elevation views for the modelled PHCSs.

600 mm. The same trend was monitored for the strengthened PHCSs, nevertheless, it was lessened, where the strengthening efficiency was enhanced as the x/s ratio increased. Fig. 17 illustrates the interaction between the opening location in respect of the x/s ratios and the ultimate loads of group I PHCSs.

Increasing the opening size without cutting extra strands did not result in a considerable reduction in both the pre-cracking stiffness and the ultimate loads of the modelled PHCSs. The extreme reductions in the ultimate loads were 3.39% and 3.89% for the unstrengthened and strengthened specimens, respectively, for an increase in the opening size from 300 × 600 mm to 600 × 600 mm.

The behaviour of the strengthened specimens was nearly identical to the unstrengthened counterparts, with an evident increase in the post-cracking stiffness reaching nearly double the original stiffness and approximately unchanged cracking loads and pre-cracking stiffness. Additionally, the considered CFRP reinforcement percentage remarkably improved the ultimate loads of the PHCSs, with an improvement reaching 69% for specimen SL1-GI-0.5S-O3-S. The load–deflection relationships for group I specimens are shown in Fig. 18.

5.1.2. *Group II*

Nine FE models were developed for group II specimens, where the average precompression was kept at 3.69 MPa. The unstrengthened specimens were provided with openings of 300 × 600 mm with x/s ratios of 0.3 and 0.5. Three CFRP reinforcement percentages were

Table 7
Summary of the investigated parameters in series (I-III).

Parameter	Series I			Series II	Series III	
	Group I	Group II	Group III		Group I	Group II
Slab cross-section ID.	PHCS160	PHCS160	PHCS160	PHCS265	PHCS400	PHCS400
x/s [a] ratios	0.2, 0.3, 0.4 & 0.5	0.3 & 0.5	0.3 & 0.5	0.3 & 0.5	0.3 & 0.5	0.3 & 0.5
Average precompression (MPa)	2.11	3.69	4.74	4.67	3.92	3.92
CFRP reinforcement percentage (ρ_c%)	0.0581	0.0581, 0.06534 & 0.07260	0.06534, 0.07985 & 0.13067	0.16542	0.18243	0.18243
Opening size	300 × 600 & 600 × 600	300 × 600	300 × 600	300 × 600	300 × 600	300 × 600
Concrete compressive strength (MPa)	40	40	40	40	40	60

[a] x is the distance between the centerlines of the opening and the near supporting plate measured along the length of the PHCS and s is the clear span of the PHCS.

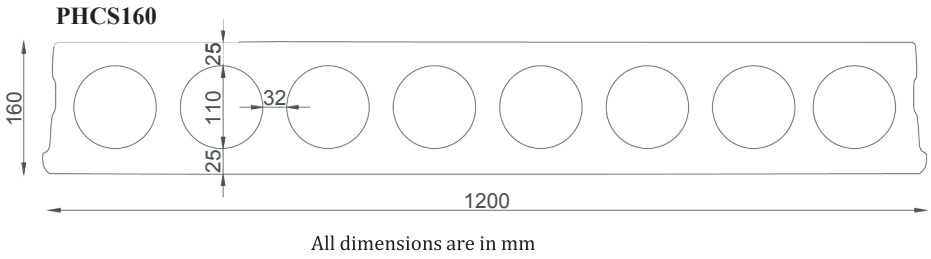

Fig. 16. Geometrical properties for PHCS160 modelled in series I specimens.

Table 8
Specimens of group I (series I).

Specimen	Average precompression (MPa)	CFRP reinforcement percentage (ρ_c%)	Openings dimensions (a × b) (mm) [a]	x/s ratio [b]	Number of strands at a general location	Number of strands at the location of an opening	P_u [c] (kN)	ΔP_{u1}% [d]	ΔP_{u2}% [e]
SL1-GI-CS	2.11	N/A	N/A	N/A	4	N/A	56.8	N/A	N/A
SL1-GI-0.2S-O3	2.11	N/A	300 × 600	0.2	4	2	54	−5	N/A
SL1-GI-0.2S-O6	2.11	N/A	600 × 600	0.2	4	2	53.1	−7	N/A
SL1-GI-0.3S-O3	2.11	N/A	300 × 600	0.3	4	2	47.2	−17	N/A
SL1-GI-0.3S-O6	2.11	N/A	600 × 600	0.3	4	2	46.1	−19	N/A
SL1-GI-0.4S-O3	2.11	N/A	300 × 600	0.4	4	2	38.4	–32	N/A
SL1-GI-0.4S-O6	2.11	N/A	600 × 600	0.4	4	2	37.1	−35	N/A
SL1-GI-0.5S-O3	2.11	N/A	300 × 600	0.5	4	2	29.3	−48	N/A
SL1-GI-0.5S-O6	2.11	N/A	600 × 600	0.5	4	2	28.7	−49	N/A
SL1-GI-0.2S-O3-S	2.11	0.0581	300 × 600	0.2	4	2	70.1	+23	+30
SL1-GI-0.2S-O6-S	2.11	0.0581	600 × 600	0.2	4	2	67.7	+19	+27
SL1-GI-0.3S-O3-S	2.11	0.0581	300 × 600	0.3	4	2	62.9	+11	+33
SL1-GI-0.3S-O6-S	2.11	0.0581	600 × 600	0.3	4	2	61.1	+8	+33
SL1-GI-0.4S-O3-S	2.11	0.0581	300 × 600	0.4	4	2	56.5	−0.5	+47
SL1-GI-0.4S-O6-S	2.11	0.0581	600 × 600	0.4	4	2	54.3	−4	+46
SL1-GI-0.5S-O3-S	2.11	0.0581	300 × 600	0.5	4	2	49.5	−13	+69
SL1-GI-0.5S-O6-S	2.11	0.0581	600 × 600	0.5	4	2	47.6	−16	+66

[a] a is the width of the opening and b is the length of the opening.
[b] x is the distance between the centerlines of the opening and the near supporting plate measured along the length of the PHCS and s is the clear span of the PHCS.
[c] The ultimate load of the specimen.
[d] The percentage change in the ultimate load compared to the control PHCS.
[e] The percentage change in the ultimate load compared to the corresponding unstrengthened specimen.

assessed for the strengthened PHCSs: 0.0581%, 0.06534% and 0.07260%. Table 9 summarizes the details of the specimens of group II.

Even though the reduction in the ultimate load was higher for a specimen with a 0.5 x/s ratio, the increase in the post-cracking stiffness for the strengthened specimens was more, resulting in higher percentage increases in the ultimate loads, compared to the corresponding unstrengthened ones.

In comparison to group I specimens, the increase in the average precompression, while keeping the CFRP reinforcement percentage constant, resulted in a reduced strengthening efficacy. This could be seen from the fact that in group II specimens, only one strand was curtailed causing slighter reductions in the ultimate loads, compared to group I specimens, however, the capacity enhancement increases were not as much as predicted.

The proposed CFRP strengthening percentages worked out to reinstate and further enhance the ultimate capacities and the post-cracking stiffness of the analysed specimens. Increases of 21% and 7% in the ultimate capacities for specimens with x/s ratios of 0.3 and 0.5 were fulfilled, respectively, compared to the control specimen without an opening.

Increasing the CFRP reinforcement percentage led to a relatively insignificant extra increase in both of the ultimate loads and the post-cracking stiffness for all of the strengthened specimens. Fig. 19 displays the load–deflection relationships for group II specimens.

5.1.3. *Group III*

Nine specimens were modelled in group III with an average precompression of 4.74 MPa. The scheme of the openings provision was exactly as that of group II (series I), nonetheless, it resulted in the curtailment of three strands.

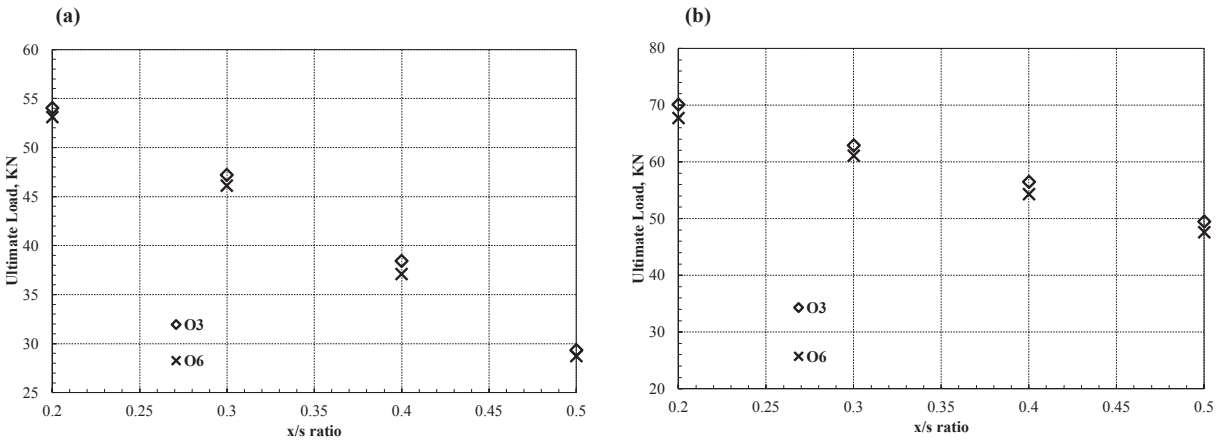

Fig. 17. Relationships between the x/s ratios and the ultimate loads for group I (series I) specimens: (a) Unstrengthened specimens and (b) Strengthened specimens.

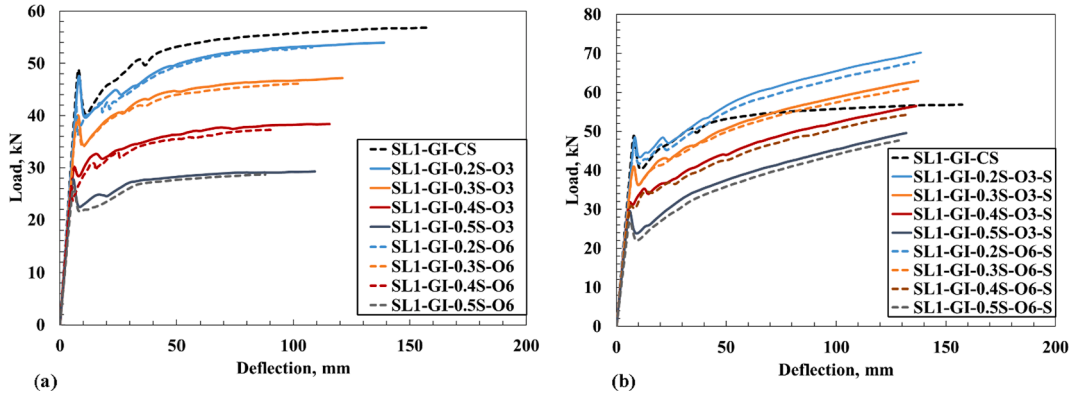

Fig. 18. Load-deflection relationships for group I (series I) specimens: (a) Control and unstrengthened specimens and (b) Control and strengthened specimens.

Table 9
Specimens of group II (series I).

Specimen	Average precompression (MPa)	CFRP reinforcement percentage (ρ_c%)	Number of strands at a general location	Number of strands at the location of an opening	P_u (kN) [a]	ΔP_{u1}%[b]	ΔP_{u2}%[c]
SL1-GII-CS	3.69	N/A	7	N/A	100.1	N/A	N/A
SL1-GII-0.3S-O3	3.69	N/A	7	6	96.6	−3	N/A
SL1-GII-0.5S-O3	3.69	N/A	7	6	85.9	−14.2	N/A
SL1-GII-0.3S-O3-S1	3.69	0.0581	7	6	116.9	+17	+21
SL1-GII-0.3S-O3-S2	3.69	0.06534	7	6	118.1	+18	+28
SL1-GII-0.3S-O3-S3	3.69	0.07260	7	6	121	+21	+32
SL1-GII-0.5S-O3-S1	3.69	0.0581	7	6	104.7	+4.3	+21.9
SL1-GII-0.5S-O3-S2	3.69	0.06534	7	6	105.5	+5.4	+22.8
SL1-GII-0.5S-O3-S3	3.69	0.07260	7	6	107	+7	+24.6

[a] The ultimate load of the specimen.
[b] The percentage change in the ultimate load compared to the control PHCS.
[c] The percentage change in the ultimate load compared to the corresponding unstrengthened specimen.

The three CFRP reinforcement percentages investigated: 0.06534%, 0.07985% and 0.13067%, managed to enhance the ultimate loads of group III specimens with x/s ratios equal to 0.3. However, this was not the case for the 0.5 x/s ratio specimens, in which reductions in the strength of 11% and 4% still persisted, compared to the control specimen.

It is worth noting that increasing the CFRP reinforcement percentage increased the ultimate load and the post cracking stiffness with a reduction in the deformation at failure, however, at a certain limit, the increase became less appreciable due to the occurrence of concrete crushing failure mode. The load–strain in concrete relationship up to failure at the maximum compression fibers is plotted in Fig. 20 for specimen SL1-GIII-0.5S-O3-S3, verifying the mode of failure encountered. Table 10 sums up the specimens of group III, and the load–deflection responses are presented in Fig. 21.

5.2. Series II

A PHCS with a thickness of 265 mm was analysed in series II. Fig. 22 shows the geometry of the PHCSs investigated in series II, for which five FE models were created. The PHCSs had an average precompression of 4.67 MPa, and were strengthened with a CFRP reinforcement percentage of 0.16542% for each specimen. The details and results of the FE models of series II specimens are introduced in Table 11.

The openings lowered the ultimate capacities of the specimens with respect to the control specimen with a maximum of 40% for an opening

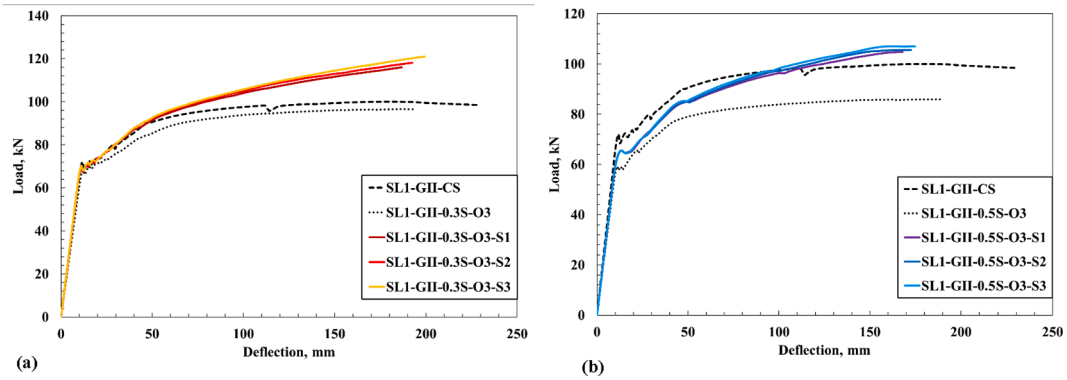

Fig. 19. Load-deflection relationships for group II (series I) specimens: (a) Control and strengthened specimens with 0.3 x/s ratio openings and (b) Control and strengthened specimens with 0.5 x/s ratio openings.

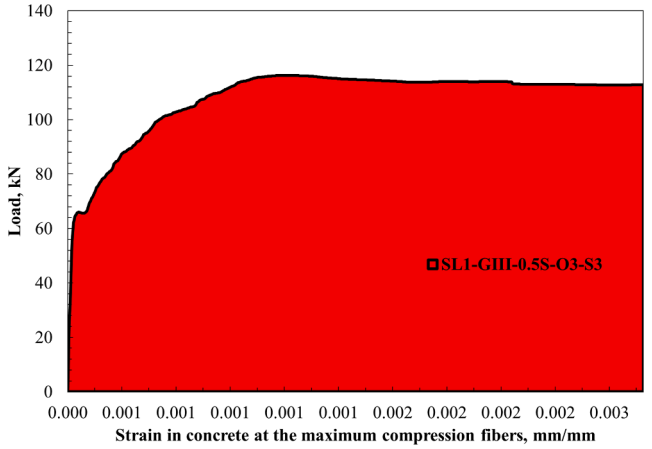

Fig. 20. Load-concrete strain at the maximum compression fibers for PHCS SL1-GIII-0.5S-O3-S3.

with a 0.5 x/s ratio.

With the increase in the thicknesses of the PHCSs modelled in series II with respect to series I, improvements in the ultimate capacities, compared to the unstrengthened counterparts reaching 29% and 54% were achieved. The ultimate load was enhanced, compared to the control specimen, for the 0.3 x/s ratio specimen with an increase of 5%, while for the PHCS with an opening of a 0.5 x/s ratio, an 8% reduction in its strength was still observed. Both of the strengthened PHCSs failed due to concrete crushing occurring at the midspan, even for the specimen with a 0.3 x/s ratio opening. A comparison of the load–deflection responses is shown in Fig. 23.

5.3. Series III

A deeper PHCS with a thickness of 400 mm was considered in this series, whose geometrical properties are shown in Fig. 24. The prestressing strands caused an average precompression of 3.92 MPa. Two values for the concrete compressive strength were chosen to assess its effect on the ultimate capacities: 40 and 60 MPa for groups I and II, respectively, while the CFRP reinforcement percentage was constant with a value of 0.18243%.

5.3.1. Group I

Group I specimens details, along with openings locations and dimensions, and the FE models' results are shown in Table 12. It was pointed out that the control slab SL3-GI-CS failed due to a sudden shear failure occurring between the loading and support plates, which agrees with previous studies [21,22] that confirmed that the relatively deep PHCSs are always more susceptible to shear failures. The shear cracks predicted by the FE model are shown in Fig. 25.

Reductions of 22% and 34% in the ultimate loads occurred concerning the unstrengthened specimens for openings with x/s ratios of 0.3 and 0.5, respectively. Interestingly, when an opening with an x/s ratio of 0.5 was introduced, the failure took place in a ductile flexural mode arising at the midspan of the PHCS SL3-GI-0.5S-O3. On the contrary, a brittle shear failure distinguished the failure of the 0.3 x/s ratio specimen.

Strengthening the specimens could not reinstate the original capacity of the control specimen, as the failure point is always limited to the strength of the concrete. A 25% reduction in the ultimate capacity was noticed for the first and a lessening of 15% was monitored for the later, but, compared to the unstrengthened specimens, 14% and 10% increases were obtained for the failure loads, respectively, without changes in the modes of failure. Fig. 26 shows the load–deflection

Table 10
Specimens of group III (series I).

Specimen	Average precompression (MPa)	CFRP reinforcement percentage (ρ_c%)	Number of strands at a general location	Number of strands at the location of an opening	P_u (kN) [a]	ΔP_{u1}% [b]	ΔP_{u2}% [c]
SL1-GIII-CS	4.74	N/A	9	N/A	126.9	N/A	N/A
SL1-GIII-0.3S-O3	4.74	N/A	9	6	113.4	−11	N/A
SL1-GIII-0.5S-O3	4.74	N/A	9	6	94.9	−25	N/A
SL1-GIII-0.3S-O3-S1	4.74	0.06534	9	6	126.5	−0.3	+12
SL1-GIII-0.3S-O3-S2	4.74	0.07985	9	6	130.4	+3	+15
SL1-GIII-0.3S-O3-S3	4.74	0.13067	9	6	136.9	+8	+21
SL1-GIII-0.5S-O3-S1	4.74	0.06534	9	6	104.9	−17	+11
SL1-GIII-0.5S-O3-S2	4.74	0.07985	9	6	106.5	−16	+12
SL1-GIII-0.5S-O3-S3	4.74	0.13067	9	6	113.4	−11	+19

[a] The ultimate load of the specimen.
[b] The percentage change in the ultimate load compared to the control PHCS.
[c] The percentage change in the ultimate load compared to the corresponding unstrengthened specimen.

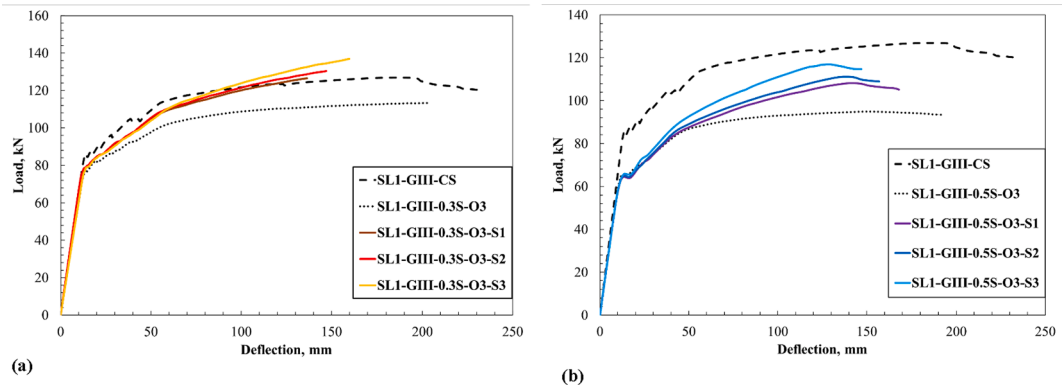

Fig. 21. Load-deflection relationships for group III (series I) specimens: (a) Control and strengthened specimens with 0.3 x/s ratio openings and (b) Control and strengthened specimens with 0.5 x/s ratio openings.

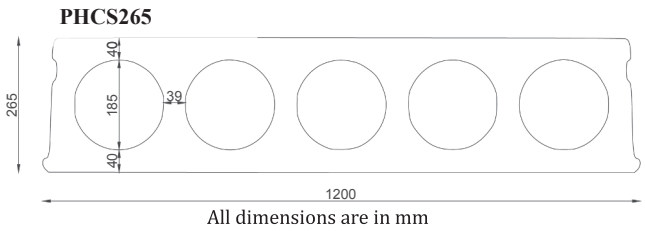

Fig. 22. Geometrical properties for PHCS265 modelled in series II specimens.

relationships for group I specimens.

5.3.2. Group II

The specimens of group I (series III) were again modeled with a higher compressive strength concrete of 60 MPa in this group. There was a slight enhancement in the reduction of the ultimate capacities for the unstrengthened PHCSs with openings, compared to group I (series III) specimens, notwithstanding, the enhancement in the ultimate capacities for the strengthened specimens did not follow the same trend. There were improvements of 19% and 25% for the strengthened specimens, compared to the unstrengthened ones for the 0.3 and 0.5 x/s ratios specimens, respectively. However, relative to the control PHCS, 4 and 16% reductions in the ultimate loads were still spotted. Fig. 27 shows the load–deflection responses for group II specimens.

It should be underlined that the failure modes were unaffected by the increase in the concrete compressive strength for the PHCSs in group II; even so, the occurrence of failure for each PHCS was noticeably delayed. Table 13 depicts the specimens details and the analysis results for group II specimens.

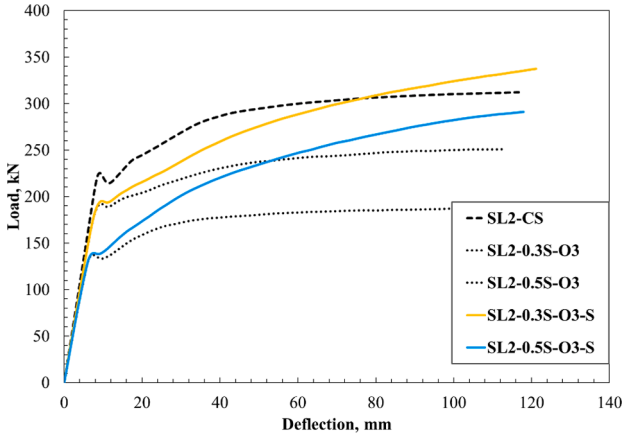

Fig. 23. Load-deflection relationships for series II specimens.

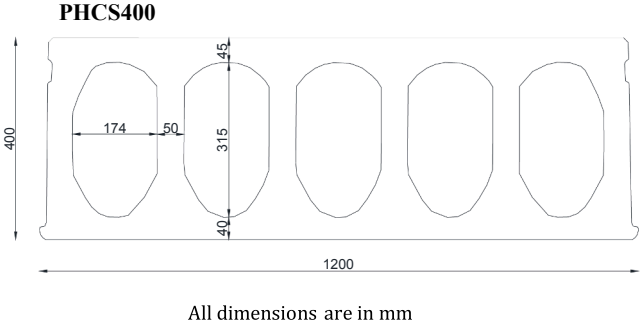

Fig. 24. Geometrical properties for PHCS400 modelled in series III specimens.

Table 11
Specimens of series II.

Specimen	Average precompression (MPa)	CFRP reinforcement percentage (ρ_c%)	Number of strands at a general location	Number of strands at location of opening	P_u (kN) [a]	ΔP_{u1}% [b]	ΔP_{u2}% [c]
SL2-CS	4.67	N/A	14	N/A	314	N/A	N/A
SL2-0.3S-O3	4.67	N/A	14	8	255	−19	N/A
SL2-0.5S-O3	4.67	N/A	14	8	188	−40	N/A
SL2-0.3S-O3-S	4.67	0.16542	14	8	330	+5	+29
SL2-0.5S-O3-S	4.67	0.16542	14	8	290	−8	+54

[a] The ultimate load of the specimen.
[b] The percentage change in the ultimate load compared to the control PHCS.
[c] The percentage change in the ultimate load compared to the corresponding unstrengthened specimen.

Table 12
Specimens of group I (series III).

Specimen	Average precompression (MPa)	CFRP reinforcement percentage (ρ_c%)	Number of strands at a general location	Number of strands at the location of an opening	P_u (kN) [a]	ΔP_{u1}% [b]	ΔP_{u2}% [c]
SL3-GI-CS	3.92	N/A	16	N/A	930	N/A	N/A
SL3-GI-0.3S-O3	3.92	N/A	16	8	721.5	−22	N/A
SL3-GI-0.5S-O3	3.92	N/A	16	8	612.5	−34	N/A
SL3-GI-0.3S-O3-S	3.92	0.18243	16	8	792.4	−15	+10
SL3-GI-0.5S-O3-S	3.92	0.18243	16	8	697.4	−25	+14

[a] The ultimate load of the specimen.
[b] The percentage change in the ultimate load compared to the control PHCS.
[c] The percentage change in the ultimate load compared to the corresponding unstrengthened specimen.

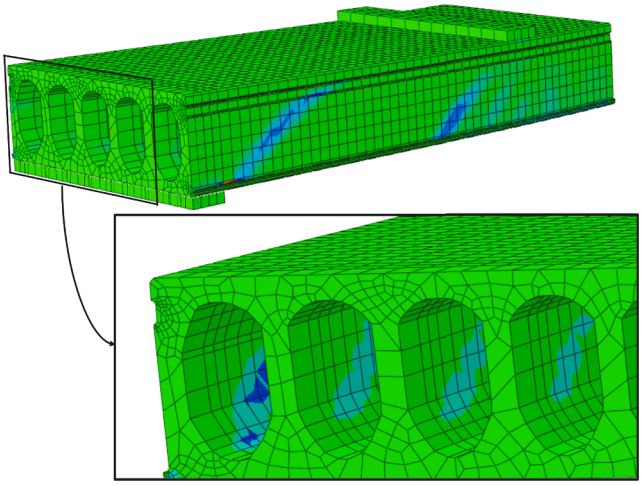

Fig. 25. Shear cracks visualization for specimen SL3-GI-CS.

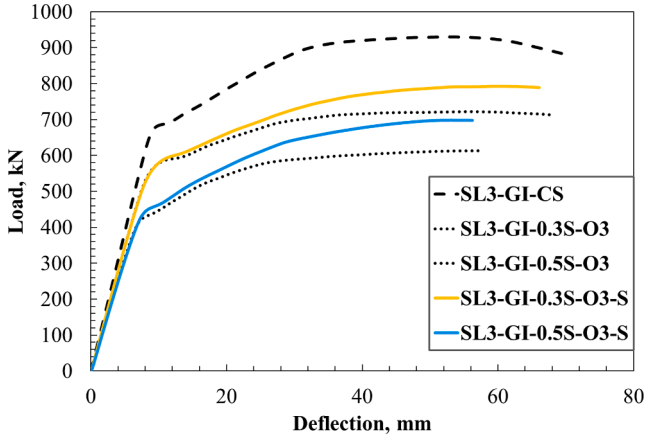

Fig. 26. Load-deflection relationships for group I (series III) specimens.

6. Summary and conclusions

In this study, three-dimensional FE models were developed to predict the behaviour of PHCSs provided with openings, with/without NSM CFRP strips strengthening. The FE models aimed to achieve accurate simulations of the aforementioned slabs by employing the CDP model to represent the non-linear concrete behaviour and taking into account the transmission length of the prestress and the bond interaction between the CFRP strips and concrete. The models were calibrated with the experimental data, and a good correlation was achieved in terms of the cracking and ultimate loads, and the corresponding deformations, as well as the PHCSs' crack patterns and failure modes.

A large-scale parametric study, with the aid of fifty FE models, was conducted afterwards to investigate the influence of the opening size

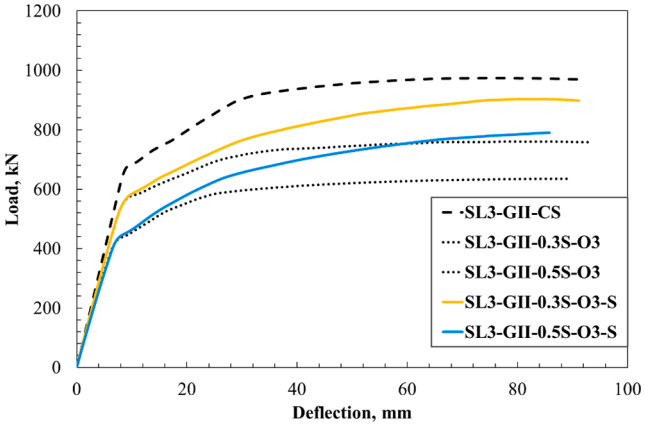

Fig. 27. Load-deflection relationships for group II (series III) specimens.

and location along the PHCS span, average precompression, CFRP reinforcement percentage, PHCS cross-sectional shape and concrete compressive strength.

Satisfying enhancements in the ultimate loads and the post-cracking stiffness for the different variations of the specimens simulated were reached, asserting the feasibility of the strengthening technique suggested for the PHCSs with capacity deficiencies due to structural openings provided.

Most importantly, utilizing the FE modelling technique proposed and the parametric study results reached, combined with future studies, could assist in the development of design guidelines for predicting the investigated PHCSs' capacities, that up to now are not present.

Eventually, the FE models' results obtained in this paper brought about the following conclusions:

- The CDP model can effectively simulate the non-linear behaviour of the concrete of the PHCSs in this study, where the crack patterns and failure modes showed fine agreements with the experimental results.
- The FE models developed in this study could predict the load–deflection responses of the PHCSs with an acceptable level of accuracy. The maximum variations in the ultimate loads and the corresponding deflections were about + 4% and −8.4%, respectively, compared to the experimental tests.
- The presence of openings in the PHCSs reduces both the strength and the stiffness of the slabs significantly. The reduction in the strength increases as the opening approaches the midspan of the PHCSs in a roughly linear relationship, with a maximum depletion of 49% encountered in this research.
- The effect of increasing the opening size has an inappreciable effect on the ultimate loads as long as the opening does not cause the cutting of additional strands. Doubling the opening width reduced the ultimate loads by a maximum of 3.39% and 3.89% for the unstrengthened and strengthened specimens of group I (series I), respectively.

Table 13
Specimens of group II (series III).

Specimen	Average precompression (MPa)	CFRP reinforcement percentage (ρ_c%)	Number of strands at a general location	Number of strands at the location of an opening	P_u (kN) [a]	ΔP_{u1}% [b]	ΔP_{u2}% [c]
SL3-GII-CS	3.92	N/A	16	N/A	941.1	N/A	N/A
SL3-GII-0.3S-O3	3.92	N/A	16	8	759.8	−19	N/A
SL3-GII-0.5S-O3	3.92	N/A	16	8	634.4	–33	N/A
SL3-GII-0.3S-O3-S	3.92	0.18243	16	8	903.2	−4	+19
SL3-GII-0.5S-O3-S	3.92	0.18243	16	8	790.6	−16	+25

[a] The ultimate load of the specimen.
[b] The percentage change in the ultimate load compared to the control PHCS.
[c] The percentage change in the ultimate load compared to the corresponding unstrengthened specimen.

- The strengthening has negligible effects on both of the cracking loads and the pre-cracking stiffness of the PHCSs under study. No matter how much is the increase in the CFRP reinforcement percentage, it can not compensate for the reduction in the cross-sectional area of the concrete, as detected in all of the PHCSs strengthened in this study.
- The post-cracking stiffness is considerably increased for the strengthened slabs, compared to the control specimens, yet after a certain limit, further increasing the CFRP reinforcement percentage has a comparatively slight improvement in the post-cracking stiffness.
- The capacity enhancement efficiency for the strengthened PHCSs is reduced by the increase of the average precompression, which led to the switch of the mode of failure to concrete crushing at the compression zone before attaining the ultimate tensile strain of the CFRP strips in the FE simulations.
- The concrete compressive strength has an appreciable impact on the efficiency of the strengthening of the PHCSs with the NSM technique. The increase in the compressive strength pushes the limit which hinders the full utilization of the FRP material. An increase of the compressive strength from 40 MPa to 60 MPa led to capacity enhancement percentages of almost 1.8 to 1.9 times that for the 40 MPa specimens, for the 60 MPa PHCSs of series III.
- Substantial attention should be paid in case of provision of openings in relatively deep PHCSs owing to the significant effect on the modes of failure of such PHCSs. In addition, they are highly susceptible to suffer sudden brittle shear failures that could not fully be evaded with the strengthening technique under discussion.

Declaration of Competing Interest

The authors declared that there is no conflict of interest.

References

[1] Pachalla SKS, Prakash SS. Experimental evaluation on effect of openings on behavior of prestressed precast hollow-core slabs. ACI Mater J 2017;114:427–36.
[2] De Lorenzis L, Teng JG. Near-surface mounted FRP reinforcement: An emerging technique for strengthening structures. Compos Part B Eng 2007;38:119–43.
[3] Elgabbas F, El-Ghandour AA, Abdelrahman AA, El-Dieb AS. Different CFRP strengthening techniques for prestressed hollow core concrete slabs: Experimental study and analytical investigation. Compos Struct 2010;92:401–11.
[4] Foubert S, Mahmoud K, El-Salakawy E. Behavior of Prestressed Hollow-Core Slabs Strengthened in Flexure with Near-Surface Mounted Carbon Fiber-Reinforced Polymer Reinforcement. J Compos Constr 2016;20.
[5] Mahmoud K, Foubert S, El-Salakawy E. Strengthening of prestressed concrete hollow-core slab openings using near-surface-mounted carbonfiber-reinforced polymer reinforcement. PCI J 2017;62:45–57.
[6] British Standards Institution. Eurocode 2: Design of concrete structures: Part 1-1: General rules and rules for buildings. British Standards Institution; 2004.
[7] Hibbitt, Karlsson, Sorensen.. ABAQUS: theory manual. Hibbitt, Karlsson & Sorensen; 1997.
[8] Lubliner J, Oliver J, Oller S, Oñate E. A plastic-damage model for concrete. Int J Solids Struct 1989;25:299–326.
[9] Lee J, Fenves GL. Plastic-damage model for cyclic loading of concrete structures. J Eng Mech 1998;124:892–900.
[10] Tamai S, Shima H, Izumo J, Okamura H. Average stress-strain in post yield range of steel bar in Concrete. Concr Libr JSCE 1988;6:117–29.
[11] Kmiecik P, Kamiński M. Modelling of reinforced concrete structures and composite structures with concrete strength degradation taken into consideration. Arch Civ Mech Eng 2011;11:623–36.
[12] Devalapura RK, Tadros MK. Stress-Strain Modeling of 270 ksi Low-Relaxation Prestressing Strands. PCI J 1992;37:100–6.
[13] Skogman BC, Tadros MK, Grasmick R. Flexural strength of prestressed concrete members. PCI J 1988;33(5):96–123.
[14] Soliman SM, El-Salakawy E, Benmokrane B. Flexural behaviour of concrete beams strengthened with near surface mounted fibre reinforced polymer bars. Can J Civ Eng 2010;37:1371–82.
[15] El-Hacha R, Rizkalla SH. Near-surface-mounted fiber-reinforced polymer reinforcements for flexural strengthening of concrete structures. ACI Struct J 2004;101:717–26.
[16] Benzeggagh ML, Kenane M. Measurement of mixed-mode delamination fracture toughness of unidirectional glass/epoxy composites with mixed-mode bending apparatus. Compos Sci Technol 1996;56:439–49.
[17] Zhang SS, Teng JG, Yu T. Bond-slip model for CFRP strips near-surface mounted to concrete. Eng Struct 2013;56:945–53.
[18] Seracino R, Raizal Saifulnaz MR, Oehlers DJ. Generic debonding resistance of EB and NSM plate-to-concrete joints. J Compos Constr 2007;11:62–70.
[19] Omran HY, El-Hacha R. Nonlinear 3D finite element modeling of RC beams strengthened with prestressed NSM-CFRP strips. Constr Build Mater 2012;31:74–85.
[20] CEB-FIP Model Code 1990 : Design Code. London :T. Telford, 1993.
[21] Yang L. Design of prestressed hollow core slabs with reference to web shear failure. J Struct Eng (United States) 1994;120:2675–96.
[22] Brunesi E, Bolognini D, Nascimbene R. Evaluation of the shear capacity of precast-prestressed hollow core slabs: numerical and experimental comparisons. Mater Struct Constr 2015;48:1503–21.